



Repositorio Institucional de la Universidad Autónoma de Madrid

<https://repositorio.uam.es>

Esta es la **versión de autor** del artículo publicado en:
This is an **author produced version** of a paper published in:

Nanoscale 12.2 (2020): 1128-1137

DOI: <https://doi.org/10.1039/C9NR07716B>

Copyright: © 2020 Royal Society of Chemistry

El acceso a la versión del editor puede requerir la suscripción del recurso

Access to the published version may require subscription

Multifunctional Carbon Nanotube Covalently Coated by Imine-based Porous Organic Polymers: Exploring Structure-Property Relationships through Nanomechanics

Alicia Moya,^[a] Marta Pérez-Illana,^[b] Mercedes Hernando-Pérez,^[b] Carmen San Martín,^[b] Julio Gómez-Herrero,^{[a],[c]} José Alemán,^{[d],[e]} Rubén Mas-Ballesté,^{*[e],[f]} Pedro J. de Pablo^{*[a],[c]}*

- (a) Dr. A. Moya, Prof. J. Gómez-Herrero, Dr. P. J. de Pablo
Department of Condense Matter Physics (module 03)
Universidad Autónoma de Madrid, 28049 Madrid (Spain)
E-mail: p.j.depablo@uam.es
- (b) M. Pérez-Illana, Dr. M. Hernando-Pérez, Dr. C. San Martín
Department of Structure of Macromolecules
Centro Nacional de Biotecnología-CSIC, 28049 Madrid (Spain)
- (c) Prof. J. Gómez-Herrero, Dr. P. J. de Pablo
Institute of Condense Matter Physics (IFIMAC)
Universidad Autónoma de Madrid, 28049 Madrid (Spain)
- (d) Dr. J. Alemán
Department of Organic Chemistry (module 01)
Universidad Autónoma de Madrid, 28049 Madrid (Spain)
E-mail: jose.aleman.lara@gmail.com
- (e) Dr. J. Alemán, Dr. R. Mas-Ballesté
Institute for Advanced Research in Chemical Sciences (IAdChem)
Universidad Autónoma de Madrid, 28049 Madrid (Spain)
E-mail: ruben.mas@uam.es
- (f) Dr. R. Mas-Ballesté
Department of Inorganic Chemistry (module 07)
Universidad Autónoma de Madrid, 28049 Madrid (Spain)

Keywords: Porous Organic Polymer, Carbon NanoTubes, Hybrid Interface, Atomic Force Microscopy, Fracture Strength

Abstract text. The assembling of 3-dimensional porous organic frameworks on the surface of carbon nanotubes have been designed and successfully developed for the first time, thought hybridization of imine-based porous organics polymer (i-POP) and oxidized MWCNT in one-pot chemical synthesis. The resulting hybrid material, ox-MWCNTs@i-POP, exhibits a conformal structure that consists in a uniform amorphous organic layer covering the ox-MWCNT surface. Insights into the mechanical fracture strength of individual hybrid nanotubes has been provided from atomic force microscopy measurements. The results

evidence a very robust hybrid tubular nanostructure that preserves the benefits from the porous organic polymer, such as CO₂ adsorption. In addition, this hybrid material presents exceptional mechanical and electrical properties, merging the properties of the CNT template and i-POP. Further digestion of the organic structure with aniline enable to study the interplay between the hybrid interface and its nanomechanics.

1. Introduction

The appeal of nanomaterials lies in their ability to downscale conventional technologies through their unique features such as large surface-to-volume ratio and their physical-chemical properties, which are often distinct from the bulk material.^[1] The possibility to anchor nanomaterials through bottom-up fabrication from molecular precursors has a large influence on their stability, performance and the ability to produce more consistent and reproducible structures.^[2] The strategy of combining two nanomaterials to form hybrids is gaining attraction for solving the current issues associated to the fabrication of nanodevices such as mechanical stability and long-term performance.^[3] The *in-situ* synthesis of nanomaterials on the surface of other nanomaterials can lead to interfacial effects as consequence of the interaction between both components, which can influence on its composition, structure, surface area and related properties.^[4,5]

Porous organic polymers (POPs) have appeared as a new promising material of microporous solids with robust carbon backbones. They form covalently bonded organic frameworks with well controlled 2D o 3D structures as a consequence of the assembling of molecular building blocks.^[6-9] The molecular units are organic molecules that react and form strong covalent bonds, which provide rigidity to form novel architectures. Design and development of POP-based hybrid structures holds interesting prospects to create hybrid materials with unprecedented properties.^[10-12] Among the possibility to hybridize POP with functional nanomaterials, carbon nanotubes (CNTs) are great candidates to be used as

templates for the POP nucleation and growth.^[13] These hybrid materials can take the advantages of the self-assembling aspects of the POP and its intrinsic chemical properties (useful for CO₂ capture, storage or catalysis)^[14,15] along with the exceptional physical properties of the CNTs (superior mechanical strength and electrical conductivity).^[16,17] The interaction between the POP building blocks and the CNTs will affect fundamental properties of these hybrid nanomaterials, determining its reactivity,^[18] and morphology.^[19] Only few examples in the literature report the synthesis of porous organic materials using nanocarbons as template (either CNTs or graphene).^[20–27] These examples used POP with 2-dimensional structure and showed the improvement of the hybrid performance for different potential applications such as catalysis, gas adsorption, batteries or supercapacitors. Although the properties of these molecular hybrids at the nanoscale are pivotal for their performance at the macroscale, their study at the single molecule level has been scarcely explored.

Mechanical properties constitute one fundamental beacon providing relevant insights about the molecular structure of nanocarbon materials, including graphene and carbon nanotubes.^[28] This issue is special relevant for CNTs, which usually requires the oxidation of its structure in order to achieve chemical functionalization. It is well-known that such oxidation induces degradation of many different properties of this material, in particular a clear decrease in the toughness of CNTs is observed upon defect creation via oxidation.^[29] Therefore, it would be highly convenient to have a chemical approximation to tune the durability of these CNTs and permit their simultaneous functionalization.

Atomic Force Microscopy (AFM) is an adequate approach for exploring molecular materials at the nanoscale in a multiple fashion, including topographical structure, electrical and mechanical properties.^[30] In fact, the nanometric tip of AFM allows the controlled manipulation of molecular materials at the nanoscale and the deformation of such nano-sized materials will allow the study of their mechanics.^[31,32] In contrast with the average information provided by bulk measurements of a large ensemble of molecules, the single

molecule approach enables to study details at the nanoscale, which may have a large influence on its macroscopic performance. For example, it is well known that the mechanical strain is an intrinsic property of a material, but it can be importantly modified as a function of defect density or grain boundaries.^[33,34] Additionally, the mechanical behaviour of a certain material strongly depends on its structure at molecular level and how the chemical bonds respond to the mechanical stress,^[35] through elastic^[36–38] or plastic^[39–41] deformations that have been measured at single molecule level. However, to the best of our knowledge, nothing is known about the effect on mechanical properties of hybridizing nanocarbons with organic materials. Therefore, we hypothesized that the encasement of ox-MWCNTs with POP would preserve and even improve the mechanical properties of the CNTs in the hybrid material, with the POP acting as a reinforcement.

In this work, a novel ox-MWCNTs@i-POP hybrid is synthesized through the *in-situ* growth, for the first time, of a 3D imine-containing organic polymer, referred as i-POP (**Figure 1a**),^[42] that conformally coats the carbon nanotubes (**Figure 1b**). This material has been characterized by electron microscopies, X-ray, Raman, RMN and FT-IR spectroscopies. In addition, their optical, electrochemical and CO₂ adsorption properties have been studied. Furthermore, this material has been manipulated using the torsional force of the AFM cantilever, which allows the quantitative study of the fracture dynamics of the hybrid nanotube in comparison with oxidized and pristine MWCNTs. These studies allow to connect the mechanical response and the structure of the material, showing that it is a great candidate for application in nanodevices such as CO₂ capture and storage.

2. Results and Discussion

2.1. Synthesis, morphology, structure and composition of the hybrid

The synthesis of a robust material bonded by strong imine bonds have been achieved by dynamic covalent chemistry between tetrakis(4-aminophenyl)methane and terephthalaldehyde,

referred as i-POP. Through bottom-up assembling of those building blocks with oxidized MWCNTs (ox-MWCNTs), we have been able to produce a hybrid nanotube structure. We thought that the oxidation of MWCNTs will facilitate the hybridization with the i-POP, through imine condensation reaction,^[43] keeping both components strongly bonded (*vide infra*). The resulting material is denoted as ox-MWCNTs@i-POP hybrid. The synthesis of this i-POP layer on the surface of p-MWCNTs was unsuccessful and resulted in the formation of POP particles randomly nucleated independently from the CNTs (**Figure S15**). This control experiment indicates that p-MWCNTs cannot act as template for the POP nucleation and suggest that for the formation of a homogeneous POP coverage, it is of the utmost importance the adequate functionalization of the MWCNTs prior to the POP synthesis.

The morphological characterisation of the ox-MWCNTs (left, **Figure 2**) and ox-MWCNTs@i-POP hybrids (right, **Figure 2**) performed using different microscopies (from top to bottom: SEM, TEM and AFM) is shown in **Figure 2a**. The relatively low magnification of the SEM data reveals a homogeneous nanostructure of the hybrid material. TEM data revealed that a well-controlled coating of the CNTs has been achieved during the *in-situ* synthesis of the organic material on the ox-MWCNTs surface. Indeed, the tubular structure of ox-MWCNTs can be clearly resolved from a conformal coating layer that uniformly cover the carbon material with a homogeneous thickness. In addition, the topographical height of the nanotube adsorbed on a solid substrate determined by AFM can be interpreted as the nanotube diameter. All microscopies reveal a conspicuous thicker diameter of the ox-MWCNTs@i-POP hybrid than the corresponding ox-MWCNTs. The thickness of the i-POP coating, measured from TEM images, ranges from 8 to 12 nm (see Supporting Information, **Figure S2**).

The diameter distribution of ox-MWCNTs and ox-MWCNTs@i-POP from an analysis of SEM, TEM and AFM images is shown in **Figure 2b**. Diameters of ox-MWCNTs and ox-MWCNTs@i-POP are of 11 ± 4 nm and 32 ± 7 nm (average \pm SD), respectively. In general, the

diameter of the ox-MWCNTs@i-POP is around three times higher than that of the ox-MWCNTs. It is worth mentioning that the diameter distribution for each technique is slightly different to the others in terms of absolute numbers. This is due to the proper limitations of sample preparation as well as the intrinsic properties of each technique.

The elemental chemical analysis of the new hybrid material is presented in **Table 1** together with those of their individual components, ox-MWCNTs and i-POP. The results show that the hybrid contains an intermediate composition between the individual materials. In addition, the nitrogen content in the hybrid material is a clear indication of the contribution of i-POP material to the hybrid composition. In order to evaluate the composition and structure of the hybrid material, we have performed Raman spectroscopy since it is a very useful technique to reveal the presence of carbon nanotubes in the hybrid structures (**Figure 3a**).^[44] In general, the spectrum of the hybrid shows the contribution of the vibrational modes of ox-MWCNTs and i-POP materials. More specifically, the hybrid contains several bands at $\sim 1163\text{ cm}^{-1}$ (C-H_{arom} from benzene rings), at $\sim 1349\text{ cm}^{-1}$ (D band of ox-MWCNTs), at $\sim 1592\text{--}1623\text{ cm}^{-1}$ (C=C from benzene rings, C=N groups from imine linkage and G band of ox-MWCNTs) and at $\sim 2696\text{ cm}^{-1}$ (2D peak of ox-MWCNTs).^[44,45]

The composition of the hybrid material has been also studied using FT-IR and NMR spectroscopies in solid state. The FT-IR spectra of the hybrid (**Figure 3b**) shows the same fingerprints than corresponding i-POP, with the most characteristic peaks of the imine linkage highlighted with a pale grey box in **Figure 3b**. These signals, observed at 1620 and 1200 cm^{-1} , correspond to C=N and C-C=N-C stretching vibrational modes,^[43] proving the formation of imine covalent bonds (see FT-IR spectra of molecular precursors in **Figure S3**). In addition, a peak at around 1700 cm^{-1} is presented in both samples, which is ascribed to aldehyde moieties from residual unreacted functional groups. The hybrid structure was further analysed by ^{13}C CP/MAS solid NMR (**Figure S4**). The assignation of the peaks, presented in **Table S1**, confirms the formation of i-POP structure. It also appears a peak at 191.97 ppm that

corresponds to aldehyde groups from non-reacted terephthaldehyde molecules, which agrees well with FT-IR results.

In addition, the crystallinity of the resulting hybrid material was evaluated by X-ray diffraction (**Figure S5**). A PXRD diffractogram of a typical amorphous material was found for the ox-MWCNTs@i-POP. To this regards, we tried to improve the crystalline of the ox-MWCNTs@i-POP material under solvothermal conditions (**Figure S6**). However, we found that the crystallization process results in the segregation of large 3D crystals of the imine material. The resulting hybrid material consists in a mixture of MWCNTs and i-POP crystals, most probably because the large 3D crystal sizes (200-500nm crystal size) cannot be folded onto the high curvature of the oxidized MWCNTs.

2.2. Mechanics of ox-MWCNTs@i-POP hybrid

The results shown above demonstrate the formation of a hybrid material with a well-controlled morphology and structure. The growth of the organic polymer has occurred on the ox-MWCNTs surface forming a uniform POP coating. Until now, we have discussed bulk techniques that cannot access to the individualized physical properties of the nanotubes. In this sense, we have studied the individual nanotubes using AFM, a convenient tool for the morphological and mechanical characterization of different materials at the nanoscale. In particular, we have studied the fracture behaviour of nanotubes with the aim of understanding the mechanics of this hybrid material at single-molecule level. We used the nano-manipulation abilities of AFM to cut individual ox-MWCNTs and hybrid nanotubes with torsional force (**Figure 4a**). First, the AFM tip establishes mechanical contact with the mica surface with a loading force of 60 nN. Afterwards the tip is dragged on the mica to induce the nanotube breakage. Subsequently, the tip releases the surface to come back to imaging mode. When the cantilever is bent and the tip is pushing on the surface, it is laterally moved at a

constant velocity of 250 nm/s while recording the normal and torsional forces. Thus, the forces during the nanotube-tip contact are monitored and combined with the AFM topographies, which enable to study its fracture mechanics. When the torsional force exerted by the tip exceeds the fracture strength, the nanotube is laterally broken. The topographies (**Figure 4b**) reveal little deformation of the tube at the fracture place, indicating that the torsional force is mostly invested in the breakage process.

Figure 4c (bottom) shows a typical lateral force-distance curve obtained during the cutting process for ox-MWCNTs@i-POP hybrid nanotube. The chart presents three differentiated behaviours. First, the curve represents the lateral force between the tip and the mica surface. The torsional force is around $\sim 2.5 \mu\text{N}$ while the loading force on the surface is about 60 nN. The second region accounts to the interaction between the tip and the tube: the lateral force presents a short jump that indicates the contact between the tip and the tube. Afterwards the torsional force increases on the stationary tube from 2.5 to $3.5 \mu\text{N}$. At this point, the static friction has been overtaken and the lateral torsion of the AFM tip induces the fracture of the nanotube. The normal force just increased 0.7 nN (see **Figure S7**), which means that the fracture was mainly caused by the torsional force. After the peak (**Figure 4c**), the lateral force decreases progressively, relaxing the accumulated torsional force and bending the extremes of the ox-MWCNTs@i-POP. Finally, the cantilever recovers the initial torsion. **Figure 4c** (top) shows the topographical profiles of the nanotube before (dark blue) and after (pale blue) its fracture.

Figure 5a shows a comparative study of all the breakage events carried out with ox-MWCNTs, ox-MWCNTs@i-POP hybrids and pristine-MWCNTs. The p-MWCNTs material was used to control how the functionalization process has an influence on their fracture resistance. Our data, as it was expected, confirms that the oxidized MWCNTs are less resistant to the fracture than the p-MWCNTs (average \pm SE of 0.7 ± 0.1 and $1.0 \pm 0.1 \mu\text{N}$, respectively). Even though CNTs are considered an extremely resistant material,^[46,47] the POP

coating the ox-MWCNTs increases the lateral force necessary for the fracture to $1.5 \pm 0.1 \mu\text{N}$. Strikingly, in the case of uncoated tubes (either pristine or oxidized) the lateral force grows with the nanotube diameter (**Figure 5b**). This interesting behaviour is related with the molecular structure of the carbon nanotubes. In the case of pristine and oxidized MWCNTs (uncoated tubes), the fracture resistance depends on the number of layers, i.e. the more walls of the nanotube (larger diameter), the higher is the lateral force required for breakage.^[48] This behaviour is consistent with the scenario where each wall-to-wall interphase acts as a barrier for the fracture propagation.^[49] Therefore, the total force required to fracture the nanotube corresponds to the sum of the forces employed to break each wall of the pristine-MWCNTs or ox-MWCNTs.

In contrast, the fracture behaviour of the ox-MWCNTs@i-POP hybrid nanotubes are not dependent on the nanotube diameter. This suggest that the mechanics of the POP coverage differs to that of the CNTs. The fact that the fracture force remains roughly constant with the POP thickness suggests that once a fracture slit is generated on the POP surface, it penetrates through the POP layer and completely breaks the material. Since the force necessary to fracture the hybrid nanotube is higher enough to fracture the MWCNTs, the whole ox-MWCNTs@i-POP hybrid nanotube is cutted. Furthermore, the interesting mechanical response to the fracture for the hybrid material can be attributed to the POP dynamic structure based on the interlocking network of covalent bond extended in three dimensions.

2.3. Multifunctional material: optical, electrochemical and CO₂ sorption properties

The mechanical-structure relationship studied above has enabled to know the features of the hybrid structure, which plays a crucial role for preserving the nanotube morphology and the exceptional physical properties of the CNTs such as robustness. Additionally, the imine-linkage POP on the CNT surface is a functional material for applications such as sensing,

photovoltaics, electrochemistry and catalysis. In this sense, we have studied several properties necessary for their conversion into a nanodevice. We have used Diffuse Reflectance Spectroscopy (DRS) and fluorimetry to study the optical properties of the materials (**Figure S8**). The absorption spectra reveal that ox-MWCNTs@i-POP absorbs light in the UV and visible range as CNTs. However, the absorption properties of the i-POP shows an abrupt absorption increase around 500 nm, which indicates that it behaves as a semiconductor with a gap energy of 2.5 eV. In addition, the emission curves for the hybrid material show the emission band centred at 537 nm, between ox-MWCNTs (533 nm) and i-POP (553 nm). From these bulk measurements, the thin semiconductor polymer layer (~8 nm) of ox-MWCNTs@i-POP material seems transparent and thus, their bulk optical properties are dominated for the nanocarbon material.

We have also performed electrochemical cyclic voltammetry (CV) for ox-MWCNTs@i-POP, ox-MWCNTs and i-POP. The CV of the i-POP material shows a very low specific current due to the low intrinsic conductivity of the material (**Figure S9**). However, the ox-MWCNTs and the hybrid material presented an important increase of the specific current at positive voltages, which is ascribed to the high electrical conductivity of the CNTs. Furthermore, the rectangular-like shape of CVs for ox-MWCNTs and hybrid samples indicates a capacitive behavior. The combination of the conductive of CNTs and insulator/semiconductor behavior of the i-POP coating results in a significant improvement of the capacitive behavior of the materials.

The nitrogen adsorption-desorption isotherms were studied for the ox-MWCNTs@i-POP hybrid material and ox-MWCNTs (**Figure S10**). Since the specific surface area of MWCNTs is very high, we found a BET surface area of ox-MWCNTs (244 m²/g). However, when such material is coated by i-POP, the BET value decreases to 74 m²/g. Moreover, the pore size distribution reveals for the hybrid material the presence of micropores (1-3 nm) characteristic of the POP structure together to mesopores (60-80 nm). This characteristic

porosity of the hybrid at the micro and mesoscale suggests its potential for hosting guests for efficient gas capture, phase separation or catalytic reactions. Therefore, we have studied the CO₂ adsorption capacity of the ox-MWCNTs@i-POP hybrid material using thermogravimetric analysis (method detailed in the experimental part). The CO₂ uptake experiment of the hybrid sample is presented in **Figure 6a**. The CO₂ adsorption properties of the ox-MWCNTs@i-POP has been compared with their individual materials at temperatures of 25, 50, 75 and 100°C (**Figure 6b**). For all the measured temperatures, the hybrid material presents a higher CO₂ sorption capacity (reported as mg CO₂ adsorbed/g of adsorbent in **Figure 6b**) than that for ox-MWCNTs and i-POP. At lower temperature, the three material behaved similarly. By contrast, at higher temperature (100 °C), the CO₂ sorption efficiency of the hybrid and i-POP material became similar and are able to adsorb more CO₂ than MWCNTs. Finally, several cycles of CO₂ adsorption-desorption were performed at 25°C without any decrease in the adsorption capacities as shown **Figure S12**, which confirms the reversibility and stable reproducibility of the CO₂ adsorption on the ox-MWCNT@i-POP. The CO₂ adsorption efficiency at the different temperatures agrees well with reported values for ox-MWCNTs and COF-nanocarbon materials.^[27,50,51] The higher affinity to CO₂ of the hybrid material in comparison with ox-MWCNTs is attributed to a more favourable CO₂-material interaction as a consequence of the presence of imine bonds in the i-POP.

Overall, optical, mechanical, electrical and adsorption properties are pointing out that this hybrid material combines the features of its individual components (MWCNT and i-POP).

2.4. Insights into the hybrid interface

In order to obtain more information about the i-POP structure, we tried to address the interface between the two components of the hybrid nanotube by chemical digestion of the i-POP. Since the i-POP formation is a reversible chemical reaction, the nucleophilic attack with

aniline reacts with the imine linkage of the POP.^[52] We stirred ox-MWCNTs@i-POP powder in aniline at 80 °C during one hour that reduced the diameter of the tubes from 29.3±0.5 nm to 9.4±0.5 nm (average ± SE) as determined by TEM analysis (**Figure 7a-b**), which is similar to uncoated ox-MWCNTs. Surprisingly, we found that the lateral force required for fracturing individual ox-MWCNTs@i-POP-digested nanotubes is higher than those necessary for uncoated CNTs, but similar to that of the initial hybrid material (**Figure S13**). Moreover, we found that this force does not depend on the diameter of the material as was observed for the initial hybrid material. The presence of imine in the ox-MWCNTs@i-POP-digested was confirmed by the observation of C=N vibrational modes at the FT-IR spectra (**Figure S14**). Interestingly, even when the sample was digested for 3 days under aniline and 80 °C, we found the same results than those observed for 1 hour digestion. All the above results indicate that the i-POP layer at the interface with the ox-MWCNTs present a different chemical composition with irreversible covalent bonds, very stable to digestion with aniline.

AFM topographical data of ox-MWCNTs, ox-MWCNTs@i-POP and ox-MWCNTs@i-POP-digested allow performing roughness analysis along the tubular structures. The Fourier transform of the topographies results in peaks that indicate the existence of repetitive grain boundaries (**Figure 7c**).^[53,54] The thick POP layer of ox-MWCNTs@i-POP material presents a significant roughness, which indicates that POP has grown in a granular structure on the CNT surface. However, the nanometric structure of the ox-MWCNTs@i-POP-digested tubes present a low roughness, similar to that of the ox-MWCNTs.

In order to put in the proper context the data obtained, it is necessary the calculation of the material fracture strength, which is an intrinsic material property and can be obtained as the ratio between the fracture force and the tip-material contact area. Estimation of such area depends on the diameter and roughness of the nanomaterial studied (using $R=2(R_{tip}/R_{NT})^{1/2}$ equation^[55]; see SI for further details). Therefore, it is possible to directly compare the estimation of fracture strength of the ox-MWCNTs@i-POP-digested, p-MWCNTs and ox-

MWCNTs, owing the similar diameters and corrugations found for this series of materials. The results (**Figure 7d**) show a strength fracture values of 0.95 ± 0.09 , 1.66 ± 0.13 and 1.63 ± 0.08 GPa (average \pm SE) for ox-MWCNTs, p-MWCNTs and ox-MWCNTs@i-POP-digested samples, respectively. The results evidence that the mechanical properties towards the fracture of the ox-MWCNTs has been improved with the POP coating up to reach fracture strength values similar to p-MWCNTs.

In summary, the data shown above clearly demonstrates a great enhancement of fracture resistance of ox-MWCNTs by the formation of a very thin layer of the i-POP, which is very stable towards chemical digestion.

3. Conclusions

This work describes the synthesis and characterization of a new 3-dimensional imine-POP material hybridized with ox-MWCNTs. A successful *in-situ* synthesis of ox-MWCNTs@i-POP hybrid material have been achieved by one-pot chemical reaction and forming a uniform coating on the ox-MWCNTs surface. The characterization of this material confirms that the composition and structure correspond to the contribution of both components of the hybrid. AFM manipulation has provided a method for observing and measuring the fracture resistance of individual tubular nanostructures, observing that hybridization with i-POP results on a mechanical reinforcement of the ox-MWCNTs. Importantly, this is the first mechanical study that explore POP structure and its hybridization with ox-MWCNTs at single-molecule scale. The chemical treatment with aniline digest the i-POP coating without complete elimination, importantly keeping its mechanical reinforcement. This suggests the formation of covalent bonds at the interface between the ox-MWCNT and i-POP. Tuning of robustness and dimensions of hybrid nanotubes can be very useful for the optimal design and manufacturing of nanodevices. Furthermore, optical, mechanical, electrical and adsorption properties are the

result of the combination of the features of its individual components (MWCNT and i-POP), and suggest the possible use of this material in nanodevices for sensing, storage or electrocatalysis.

4. Experimental Section

Synthesis procedure: A 15 mL ethanolic mixture of tetrakis(4-amino-phenyl)methane (30 mg) with terephthalaldehyde (21.8 mg) and acetic acid (10 μ L) are mixed with a dispersion of 5 mg of ox-MWCNTs – either pristine or oxidized – in ethanol (15 mL). The mixture was stirred overnight at ambient conditions. The precipitate was obtained by vacuum filtration, washed with ethanol and dried in vacuum for 24 hours. Same procedure was used to produce a referenced POP material except for the incorporation of CNTs. The crystallization process was performed to the hybrid material under hydrothermal condition using same amounts of building block and nanocarbons and a solvent mixture of mesylene:dioxano (1:9) during several hours (from 1 to 72 h) and at 120°C. Also, a re-growth from the amorphous material was carried out under the same hydrothermal conditions. The nucleophilic attach to the imine covalent bond was performed by 1 hour and also, extended to 3 days stirring of ox-MWCNTs@i-POP sample in aniline at 80 °C. All the chemical reagents, solvents and building blocks were purchased by Sigma-Aldrich. The oxidized MWCNTs were purchased to Nanocyl Ltd.

Morphological and structural characterization: Morphological characterization of the materials was carried out using a scanning electron microscope (Philips XL30 S-FEG) at 2.5 keV and transmission electron microscope (JEOL JEM 1011 with Gatan ES1000Ww camera) operating at 100 keV. Measurements of the nanotube diameter were done using ImageJ

software. Crystallinity was studied using X-Ray Diffraction (XRD), Panalytical X'pert PRO. FT-IR spectroscopy was used to evaluate structural features of the different materials using an Agilent Cary 630 FTIR spectrometer in Attenuated Total Reflectance (ATR) mode. The chemical structure of the hybrid material was also analysed by solid NMR spectroscopy in a Bruker AV 400 WB spectrometer running at 300 MHz for ^{13}C . Raman spectroscopy was performed to analyze the features of both materials but especially, those of the CNTs using a Renishaw PLC spectrometer with 532 nm wavelength laser-excitation, 1 μm spot size and 0.5 mW of power. The chemical composition was obtained by Elemental Analyzed LECO CHNS-932. Electrochemical experiments were performed under argon atmosphere at RT in aqueous solution (NaClO_4) as supporting electrolytes. Measurements were carried out with an Ivium CompaqStat potentiostat interfaced with a computer. A standard three-electrode electrochemical cell was used. Potentials are referred to an Ag/AgCl. The working electrode was a Pt wire and the auxiliary electrode consisted in 1 mg of the sample deposited on glassy carbon electrode. The optical features of the samples (absorption and emission spectra) were analyzed using UV-Vis Diffuse Reflectance Spectroscopy (DRS). Absorption studies were obtained in the range of 250–700 nm by UNICAM. Emission spectra of solid samples were measured in a Fluorescence Spectrofluorometer Jasco FP-800, using 450nm as excitation wavelength. Adsorption–desorption isotherms were carried out on Micrometrics ASAP 2010 at 77K with N_2 as adsorbate. Specific surface area (according to BET) and porosity (according to BJH) were determined assuming 0.162 nm^2 as the nitrogen molecule area.

Thermogravimetric analysis: Thermogravimetric analysis (TGA) were performed using TA Instruments TGA Q500 (TA Instruments, New Castle, USA) with a ramp of 5 $^\circ\text{C}/\text{min}$ under Ar gas from room temperature to 800 $^\circ\text{C}$. For CO_2 adsorption experiments, Ar and CO_2 were used as the purge and furnace gases at the flow rates of 90 mL/min. In order to dehydrate and

degas the samples prior CO₂ adsorption, the temperature of the furnace was raised to 100 °C at the rate of 5 °C/min, then the temperature was down to room temperature and after verification of stable weight, the furnace gas was changed to CO₂. At each temperature (25, 50, 75 and 100 °C), an isotherm of 60 minutes was performed. Cycling test was performed by a similar method at 25 °C. As initial step, the sample was heated to 100 °C under Ar atmosphere and results in a mass decrease due the presence of moisture in the sample. Once a constant mass was achieved, the temperature was reduced to a set level of 25°C and the flow gas was switched to CO₂. After an isotherm of 60 minutes, temperature was increased by steps of 25°C up to 125°C, observing a mass decrease since temperature facilitates the CO₂ desorption process.

AFM characterization: The AFM imaging and nanomechanical measurements were evaluated using an atomic force microscope (Nanotec Electrónica) operating in dynamic mode.^[56] The AFM was housed inside a temperature-controlled chamber (18 °C). All the experiments were carried out with rectangular silicon nitride AFM cantilevers (RC800PSA, Olympus, Tokyo, Japan) with nominal length of 100 µm, width of 20 µm and thickness of 800 nm. The employed AFM probes have a nominal spring constant of 0.35 N/m and were routinely calibrated using the Sader's method.^[57] The lateral force applied to the AFM tip was calibrated using a TGZ1 silicon grating^[58] and the lateral spring constant was calculated using the formula: $K_N/K_L = \frac{1}{2} (h/l)^2$ being K_N and K_L the normal and lateral spring constant, h the tip height and l the length of the cantilever.^[59] More information about the calibration of the lateral force can be found in the supplementary information (**Figure S1**). The tip radii of our AFM probes were estimated to be 15 nm based on the shift observed between the topographical curve and the lateral force curve when measuring the calibration Si-grating. For evaluation of the fracture mechanics of the nanotubes, a script was developed in WSxM

software to draw a path line, through which the AFM tip will be moved at a constant speed of 250 nm/s and an indentation of 200 nm (60 nN). Lateral and normal forces curves were recorded for the forward indentation, lateral displacement and backward indentation. Furthermore, images before and after the tip lateral displacement were acquired. All the obtained images and curves were processed using the WSxM software.^[60]

For adsorption of the samples, 10 µL of the sample dispersion (1%wt. in ethanol, sonication of 1 hour) were deposited on a mica flat surface. The non-adsorbed particles and contaminants were removed by drying the sample with N₂.

Acknowledgements

We thank the Spanish Government (RTI2018-095038-B-I00), “Comunidad de Madrid” and European Structural Funds (S2018/NMT-4367). P. D. -L. thanks CAM for a postdoctoral contract (2016-T2/IND-1660).

References

- [1] N. K. Sunita Kumbhat, *Essentials in Nanoscience and Nanotechnology*, John Wiley & Sons, Ltd, **2016**.
- [2] N. T. K. Thanh, N. Maclean, S. Mahiddine, *Chem. Rev.* **2014**, *114*, 7610–7630.
- [3] Eder Dominik, Schlögl Robert, *Nanocarbon-Inorganic Hybrids, Next Generation Composites for Sustainable Energy Applications*, De Gruyter, Berlin, Boston, **2014**.
- [4] I. M. Tidswell, N. M. Marković, P. N. Ross, *Surf. Sci.* **1994**, *317*, 241–252.
- [5] R. Subbaraman, D. Tripkovic, D. Strmcnik, K.-C. Chang, M. Uchimura, A. P. Paulikas, V. Stamenkovic, N. M. Markovic, *Science* **2011**, *334*, 1256.

- [6] L. D. Belyakova, A. V. Kiselev, N. P. Platonova, T. I. Shevchenko, *Adv. Colloid Interface Sci.* **1984**, *21*, 55–118.
- [7] S. Das, P. Heasman, T. Ben, S. Qiu, *Chem. Rev.* **2017**, *117*, 1515–1563.
- [8] A. P. Côté, A. I. Benin, N. W. Ockwig, M. O’Keeffe, A. J. Matzger, O. M. Yaghi, *Science* **2005**, *310*, 1166.
- [9] H. Bildirir, V. G. Gregoriou, A. Avgeropoulos, U. Scherf, C. L. Chochos, *Mater. Horiz.* **2017**, *4*, 546–556.
- [10] Y. Peng, M. Zhao, B. Chen, Z. Zhang, Y. Huang, F. Dai, Z. Lai, X. Cui, C. Tan, H. Zhang, *Adv. Mater.* **2018**, *30*, 1705454.
- [11] P. Pachfule, M. K. Panda, S. Kandambeth, S. M. Shivaprasad, D. D. Díaz, R. Banerjee, *J. Mater. Chem. A* **2014**, *2*, 7944–7952.
- [12] B. P. Biswal, H. D. Chaudhari, R. Banerjee, U. K. Kharul, *Chem. – Eur. J.* **2016**, *22*, 4695–4699.
- [13] J. J. Vilatela, D. Eder, *ChemSusChem* **2012**, *5*, 441–441.
- [14] W. Wang, M. Zhou, D. Yuan, *J. Mater. Chem. A* **2017**, *5*, 1334–1347.
- [15] N. Enjamuri, S. Sarkar, B. M. Reddy, J. Mondal, *Chem. Rec.* **2018**, *0*, DOI 10.1002/tcr.201800080.
- [16] A. A. Balandin, *Nat. Mater.* **2011**, *10*, 569.
- [17] B. Peng, M. Locascio, P. Zapol, S. Li, S. L. Mielke, G. C. Schatz, H. D. Espinosa, *Nat. Nanotechnol.* **2008**, *3*, 626.
- [18] D. Tasis, N. Tagmatarchis, A. Bianco, M. Prato, *Chem. Rev.* **2006**, *106*, 1105–1136.
- [19] C. J. Shearer, A. Cherevan, D. Eder, *Adv. Mater.* **2014**, *26*, 2295–2318.
- [20] A. B. Soliman, R. R. Haikal, Y. S. Hassan, M. H. Alkordi, *Chem. Commun.* **2016**, *52*, 12032–12035.
- [21] B. Sun, J. Liu, A. Cao, W. Song, D. Wang, *Chem. Commun.* **2017**, *53*, 6303–6306.

- [22] J. Sun, A. Klechikov, C. Moise, M. Prodana, M. Enachescu, A. V. Talyzin, *Angew. Chem. Int. Ed.* **2018**, *57*, 1034–1038.
- [23] F. Xu, S. Jin, H. Zhong, D. Wu, X. Yang, X. Chen, H. Wei, R. Fu, D. Jiang, *Sci. Rep.* **2015**, *5*, 8225.
- [24] P. Wang, Q. Wu, L. Han, S. Wang, S. Fang, Z. Zhang, S. Sun, *RSC Adv.* **2015**, *5*, 27290–27294.
- [25] X. Zhang, Z. Wang, L. Yao, Y. Mai, J. Liu, X. Hua, H. Wei, *Mater. Lett.* **2018**, *213*, 143–147.
- [26] J. Yoo, S. Lee, S. Hirata, C. Kim, C. K. Lee, T. Shiraki, N. Nakashima, J. K. Shim, *Chem. Lett.* **2015**, *44*, 560–562.
- [27] J. Yoo, S.-J. Cho, G. Y. Jung, S. H. Kim, K.-H. Choi, J.-H. Kim, C. K. Lee, S. K. Kwak, S.-Y. Lee, *Nano Lett.* **2016**, *16*, 3292–3300.
- [28] D. G. Papageorgiou, I. A. Kinloch, R. J. Young, *Prog. Mater. Sci.* **2017**, *90*, 75–127.
- [29] A. Garg, S. B. Sinnott, *Chem. Phys. Lett.* **1998**, *295*, 273–278.
- [30] M. Marrese, V. Guarino, L. Ambrosio, *J. Funct. Biomater.* **2017**, *8*, 7.
- [31] S.-C. Yang, X. Qian, *Langmuir* **2013**, *29*, 11793–11801.
- [32] E. W. Wong, P. E. Sheehan, C. M. Lieber, *Science* **1997**, *277*, 1971.
- [33] J. P. Hirth, *Metall. Trans.* **1972**, *3*, 3047–3067.
- [34] N. Ding, C.-M. L. Wu, H. Li, *Phys. Chem. Chem. Phys.* **2014**, *16*, 23716–23722.
- [35] L. Xu, N. Wei, Y. Zheng, *Nanotechnology* **2013**, *24*, 505703.
- [36] T. Hertel, R. Martel, P. Avouris, *J. Phys. Chem. B* **1998**, *102*, 910–915.
- [37] M.-F. Yu, O. Lourie, M. J. Dyer, K. Moloni, T. F. Kelly, R. S. Ruoff, *Science* **2000**, *287*, 637.
- [38] M. C. Strus, R. R. Lahiji, P. Ares, V. López, A. Raman, R. Reifengerger, *Nanotechnology* **2009**, *20*, 385709.

- [39] M. R. Falvo, R. M. Taylor II, A. Helser, V. Chi, F. P. Brooks Jr, S. Washburn, R. Superfine, *Nature* **1999**, 397, 236.
- [40] M. Zheng, X. Chen, C. Park, C. C. Fay, N. M. Pugno, C. Ke, *Nanotechnology* **2013**, 24, 505719.
- [41] H.-J. Kim, K. H. Kang, D.-E. Kim, *Nanoscale* **2013**, 5, 6081–6087.
- [42] J. Alemán, S. Cabrera, R. Mas-Ballesté, A. Jiménez-Almarza, A. López-Magano, L. Marzo, *ChemCatChem* **2019**, 0, DOI 10.1002/cctc.201901061.
- [43] F. J. Uribe-Romo, J. R. Hunt, H. Furukawa, C. Klöck, M. O’Keeffe, O. M. Yaghi, *J. Am. Chem. Soc.* **2009**, 131, 4570–4571.
- [44] M. S. Dresselhaus, G. Dresselhaus, R. Saito, A. Jorio, *Phys. Rep.* **2005**, 409, 47–99.
- [45] Z. Lei, Q. Yang, Y. Xu, S. Guo, W. Sun, H. Liu, L.-P. Lv, Y. Zhang, Y. Wang, *Nat. Commun.* **2018**, 9, 576.
- [46] J.-P. Salvetat, J.-M. Bonard, N. H. Thomson, A. J. Kulik, L. Forró, W. Benoit, L. Zuppiroli, *Appl. Phys. A* **1999**, 69, 255–260.
- [47] T. Kuzumaki, Y. Mitsuda, *Jpn. J. Appl. Phys.* **2006**, 45, 364–368.
- [48] K. M. Liew, X. Q. He, C. H. Wong, *Acta Mater.* **2004**, 52, 2521–2527.
- [49] B. Chen, S. Li, H. Imai, J. Umeda, M. Takahashi, K. Kondoh, *Micron* **2015**, 69, 1–5.
- [50] K. Osler, D. Dheda, J. Ngoy, N. Wagner, M. O. Daramola, *Int. J. Coal Sci. Technol.* **2017**, 4, 41–49.
- [51] J. Yoo, S. Lee, C. K. Lee, C. Kim, T. Fujigaya, H. J. Park, N. Nakashima, J. K. Shim, *RSC Adv.* **2014**, 4, 49614–49619.
- [52] T. Ma, E. A. Kapustin, S. X. Yin, L. Liang, Z. Zhou, J. Niu, L.-H. Li, Y. Wang, J. Su, J. Li, et al., *Science* **2018**, 361, 48.
- [53] P. Klapetek, I. Ohlídal, K. Navrátil, *Microchim. Acta* **2004**, 147, 175–180.
- [54] F. El Feninat, S. Elouatik, T. H. Ellis, E. Sacher, I. Stangel, *Appl. Surf. Sci.* **2001**, 183, 205–215.

- [55] E. Gnecco, A. Rao, K. Mougín, G. Chandrasekar, E. Meyer, *Nanotechnology* **2010**, *21*, 215702.
- [56] P. J. de Pablo, J. Colchero, M. Luna, J. Gómez-Herrero, A. M. Baró, *Phys. Rev. B* **2000**, *61*, 14179–14183.
- [57] J. E. Sader, J. W. M. Chon, P. Mulvaney, *Rev. Sci. Instrum.* **1999**, *70*, 3967–3969.
- [58] **N.d.**
- [59] Jaime Colchero, Reibungskraftmikroskopie, Universität Konstanz, **1993**.
- [60] I. Horcas, R. Fernández, J. M. Gómez-Rodríguez, J. Colchero, J. Gómez-Herrero, A. M. Baro, *Rev. Sci. Instrum.* **2007**, *78*, 013705.

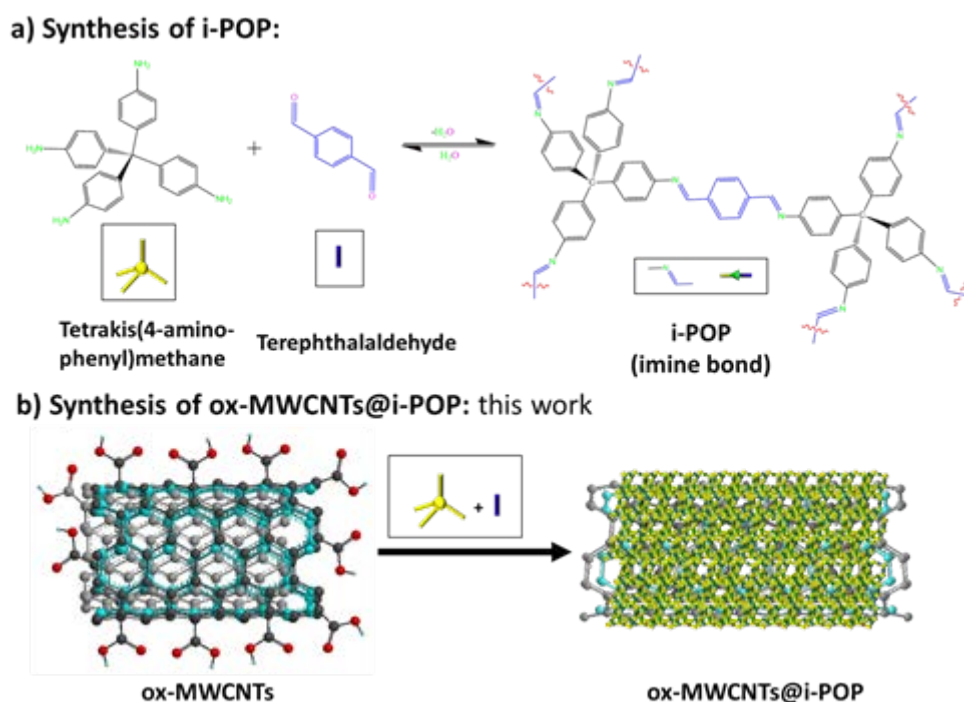


Figure 1. Schematic representation of a) the synthesis of i-POP, constructed from two organic building blocks (amine and aldehyde) linked by imine bonds and b) synthesis strategy of this work to combine organic building blocks with ox-MWCNTs.

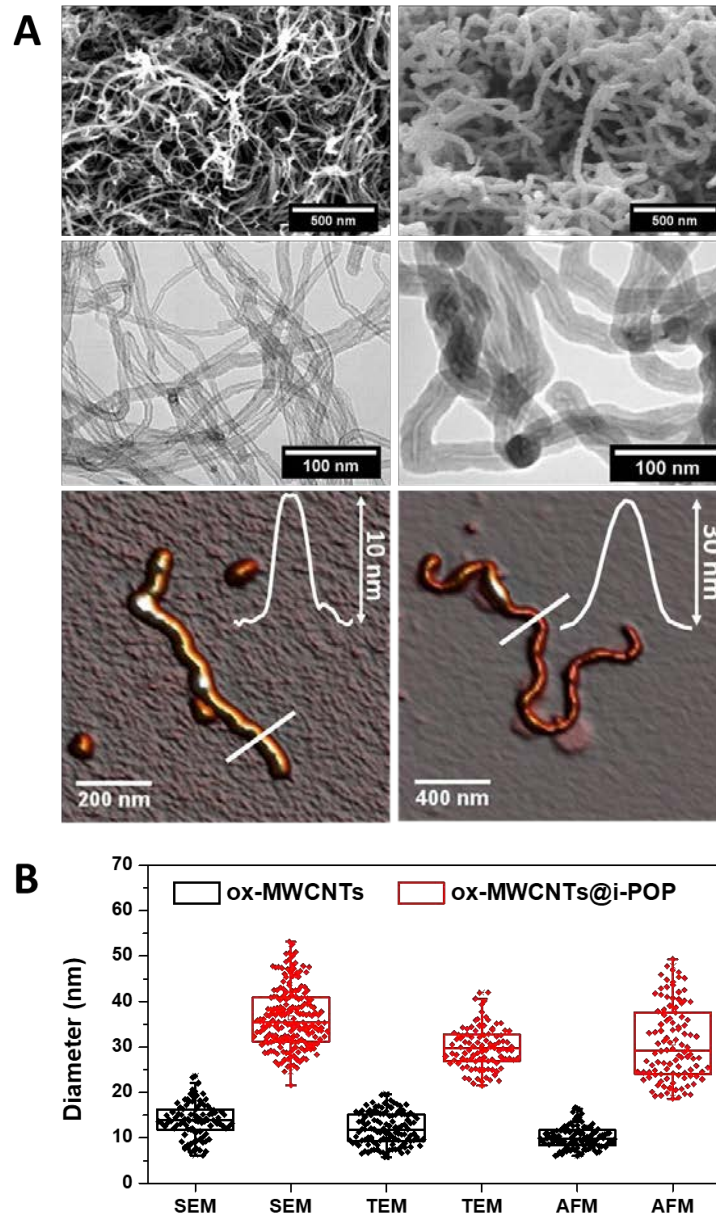


Figure 2. Nanotube morphology. a) From top to bottom: SEM, TEM and AFM images of ox-MWCNTs (left images) and ox-MWCNTs@i-POP hybrid materials (right images). b) Box chart of diameter distribution of ox-MWCNTs (black) and ox-MWCNTs@i-POP hybrids (red) measured from SEM, TEM and AFM images.

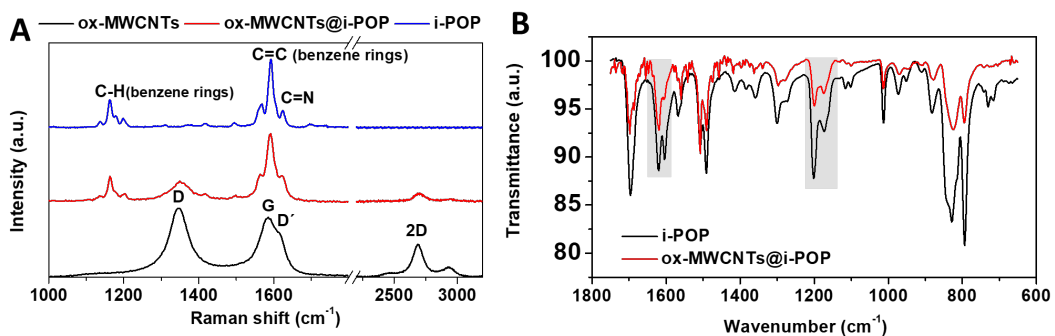


Figure 3. Structural characterization. a) Raman spectra showing the vibrational structure of ox-MWCNTs@i-POP in comparison with its individual components (their characteristic

Raman modes are highlighted in the graph). b) FT-IR spectra of as-synthesized i-POP and ox-MWCNTs@i-POP. Pale grey boxes indicate the features of the imine linkage, the C=N (at 1620 cm^{-1}) and C-C=N-C (at 1200 cm^{-1}) stretching vibrational modes.

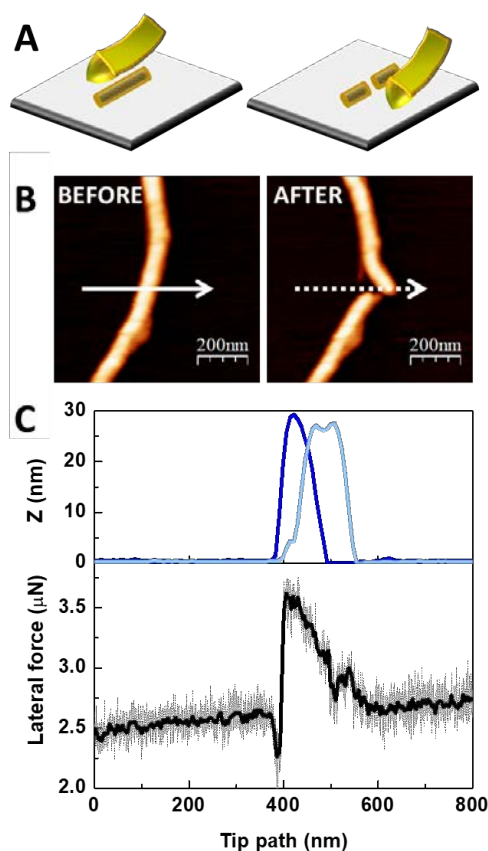


Figure 4. Fracture experiments. a) Representation of the breakage process for an individual nanotube using the torsional force of the AFM probe. b) Topographical images before (left) and after (right) the breakage of a ox-MWCNTs@i-POP hybrid nanotube, indicating the path length of the AFM tip with a white arrow. c) Top: topographical profile before (dark blue) and after (pale blue) the nanotube fracture and bottom: lateral force as a function of the path of the AFM tip.

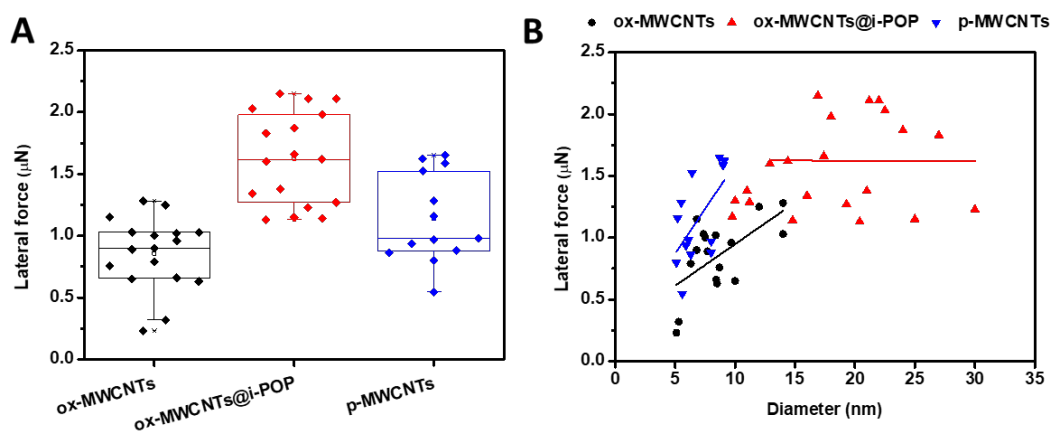


Figure 5. Mechanical behaviour of nanotubes. a) Box chart of lateral force applied by AFM tip to cut individual nanotubes. b) Effect of the diameter in the lateral force for cutting nanotubes of ox-MWCNTs, ox-MWCNTs@i-POP and p-MWCNTs as a reference.

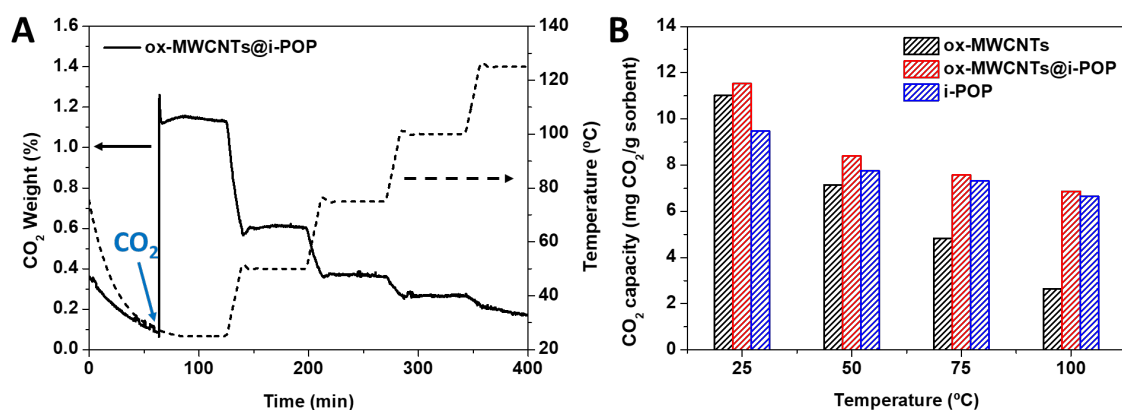


Figure 6. CO₂ uptake. a) TGA showing mass changes due to the CO₂ adsorption obtained from the ox-MWCNTs (black line) and ox-MWCNTs@i-POP (red line). Black dashed line indicates the temperature of the experiment. b) CO₂ sorption capacity of the hybrid material and its individual components.

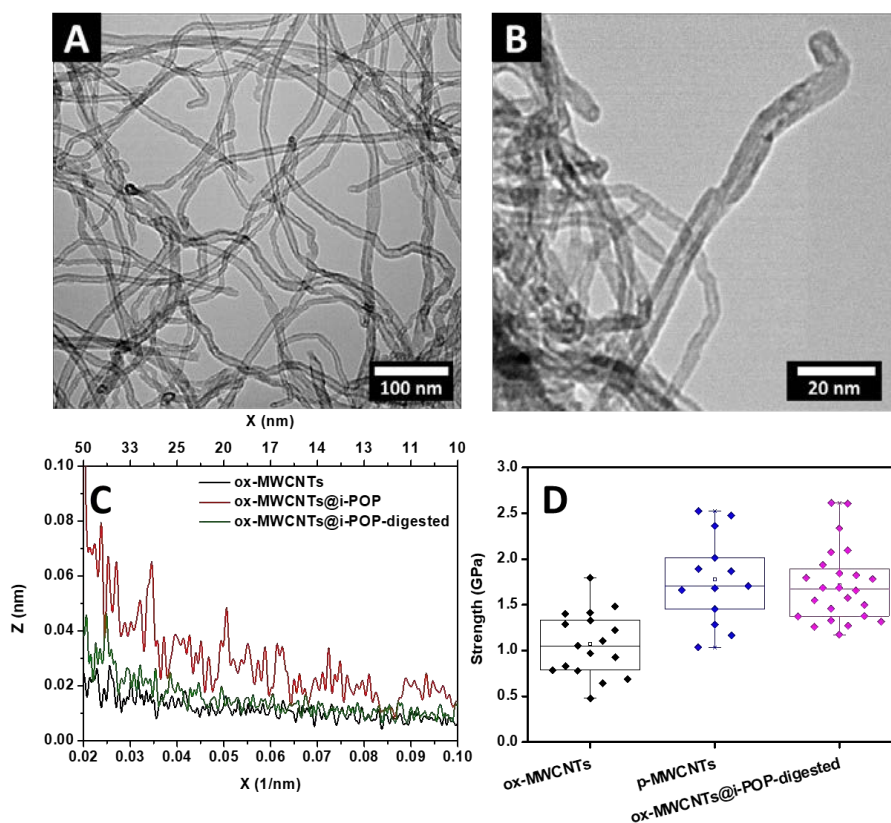


Figure 8. Digestion of ox-MWCNTs@i-POP hybrids. a,b) TEM images of ox-MWCNTs@i-POP-digested showing the decrease of the hybrid nanotube diameter c) roughness measured by FFT of nanotube topographies measured by AFM as function of the length profile and d) fracture strength calculated from the lateral force measured during the breaking events.

Table 1. Content in atomic percent of C, H and N for ox-MWCNTs, i-POP and ox-MWCNTs@i-POP hybrid.

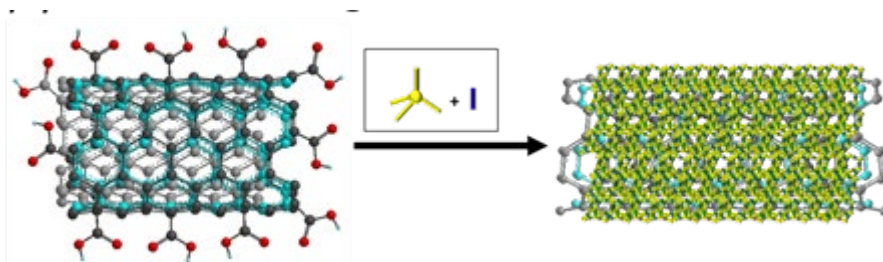
| Sample | %C | %H | %N |
|-----------------|-------|------|------|
| ox-MWCNTs | 87.7 | 0.46 | 0.17 |
| i-POP | 79.86 | 5.22 | 8.41 |
| ox-MWCNTs@i-POP | 81.7 | 4.34 | 7.52 |

Keywords

Porous Organic Polymer, Carbon NanoTubes, Hybrid Interface, Atomic Force Microscopy, Fracture Strength

Carbon Nanotube Covalently Coated by Imine-based Porous Organic Polymers: Exploring Structure-Property Relationships through Nanomechanics

ToC figure ((Please choose one size: 55 mm broad \times 50 mm high **or** 110 mm broad \times 20 mm high. Please do not use any other dimensions))



Supporting Information

Carbon Nanotube Covalently Coated by Imine-based Porous Organic Polymers: Exploring Structure-Property Relationships through Nanomechanics

*Alicia Moya,^[a] Marta Pérez-Illana,^[b] Mercedes Hernando-Pérez,^[b] Carmen San Martín,^[b]
Julio Gómez-Herrero,^{[a],[c]} José Alemán,*^{[d],[e]} Rubén Mas-Ballesté,*^{[e],[f]} Pedro J. de
Pablo*^{[a],[c]}*

Calibration of the AFM and cantilever spring constant: A simple method to calibrate the frictional force from lateral force and topographical images using an atomic force microscope has been performed using a rectangular silicon nitride AFM cantilevers with the following dimensions: 800 nm thick, 100 μm long and 20 μm wide. Its normal spring constant and frequency resonance is routinely calibrated using Sader's method^[44] before all the experiments and obtaining values of 68-74 kHz and 0.29-0.35 N/m, respectively. From the formula described in experimental section, we obtain the lateral spring constant of the cantilever, $K_L = 690\text{-}832$ N/m, which will be used for the calibration of the frictional force.

When the tip is laterally moving, the focused laser on the cantilever changes its angle of reflection on the photodetector. These changes are registered by a voltage signal, which must be calibrated into force units. For such propose, the lateral calibration factor was determined using Si-grating with step heights of 20.3 ± 1.5 nm height. Lateral force images were acquired for such a grid and converted into force curves to calculate the lateral calibration factor. For example, the graph in **Figure S1** shows the increase of the lateral force when the AFM tip touches the step of the grid and, from this slope, we obtain a calibration factor in units of V/nm. The calibrated value obtained from different lateral forces images results 0.022 V/nm. Finally, the voltage signal of the lateral force is converted to Newtons using the lateral spring constant and the above calibrated value.

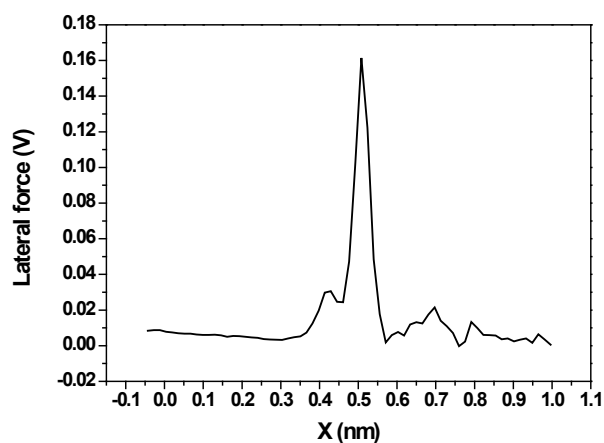


Figure S1. Lateral force curve obtained from the lateral force image of a Si-grid of 20 nm.

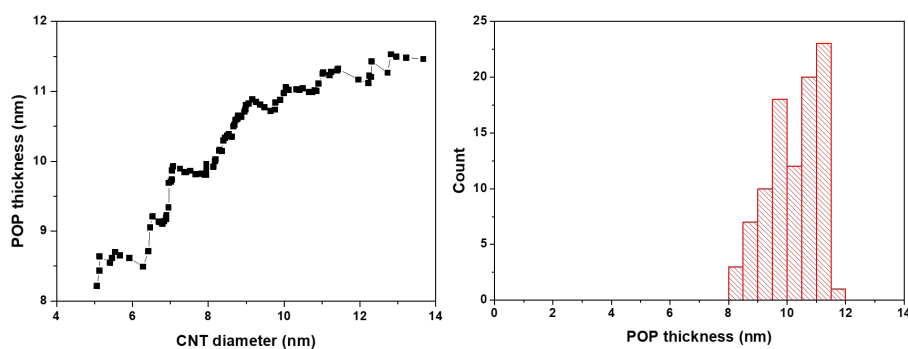


Figure S2. Left: Relation between the POP thickness and the CNT diameter. Right: Distribution of the POP thickness measured from TEM images.

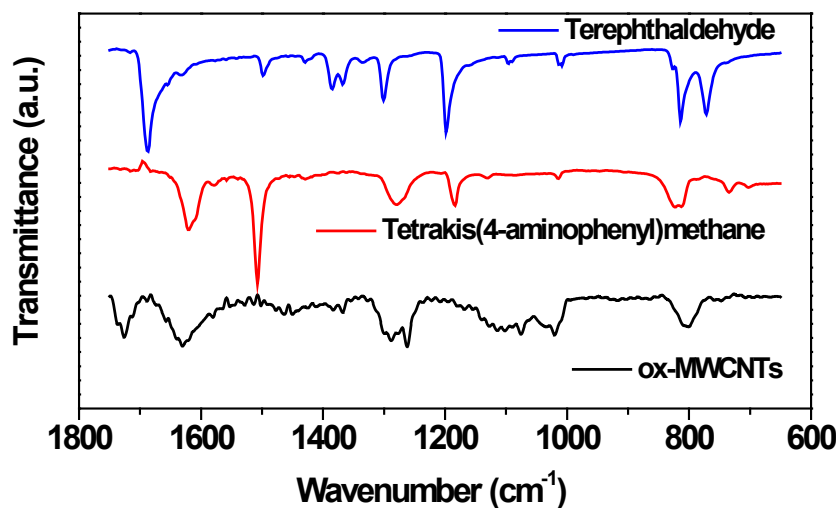


Figure S3. FT-IR spectra of ox-MWCNTs (black curve) and POP precursors: tetrakis(4-aminophenyl)methane (red curve) and terephthalaldehyde (green curve).

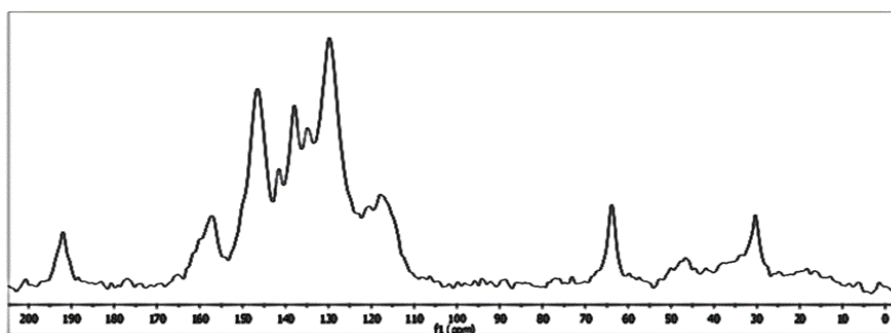


Figure S4. Solid-state ^{13}C CP-MAS spectrum of synthesized ox-MWCNTs@i-POP hybrid material. The characteristic chemical ^{13}C -NMR shifts in ppm hybrid are assigned in the table below.

Table S1. Signal assignment of ^{13}C -NMR spectra of **Figure S4**.

| Signal | Assignment |
|--------|-----------------------------------------------|
| 30.33 | Solvent |
| 63.84 | Aliphatic quaternary: α -aromatic |
| 117.89 | Aromatic: β -aliphatic, γ -imine |
| 129.77 | Aromatic: β -vinyl |
| 134.9 | Aromatic: α -aliphatic, p -imine |
| 137.94 | Aromatic: α -vinyl |
| 141.53 | Aromatic: α -carbonyl |
| 146.54 | Aromatic: β -imine, γ -aliphatic |
| 157.23 | Alkene: α -imine, α -aromatic |
| 191.97 | Carbonyl: α -aromatic |

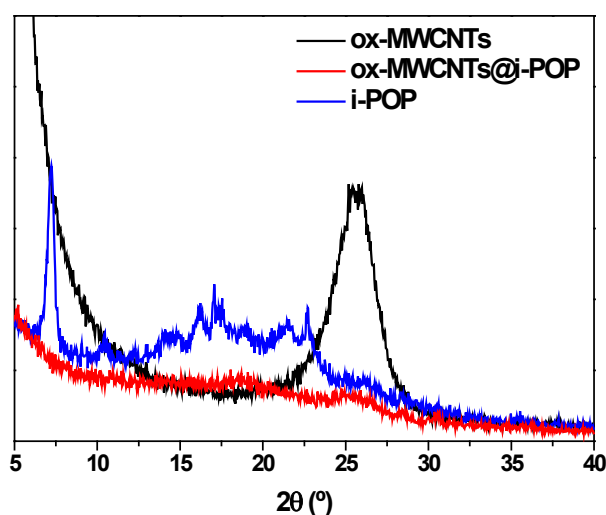


Figure S5. X-ray diffraction pattern of ox-MWCNTs and ox-MWCNTs@i-POP hybrid material.

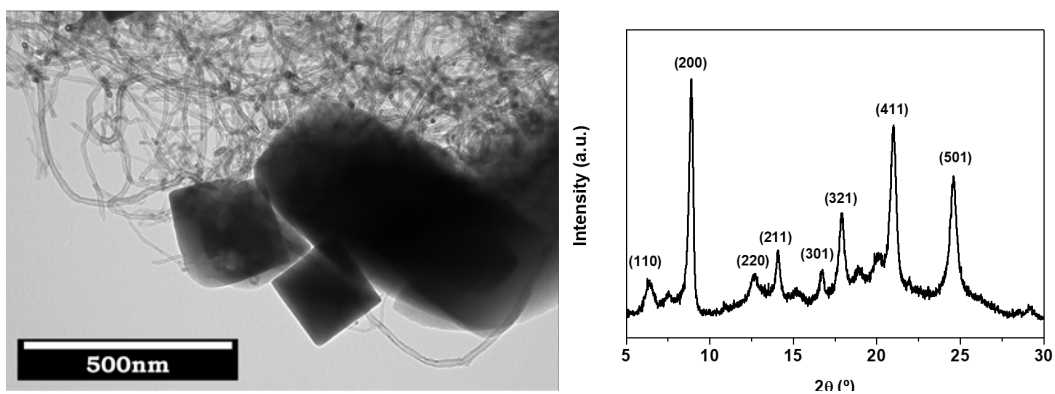


Figure S6. TEM image of the crystallized ox-MWCNTs@i-POP material (left) its corresponding XRD pattern (right).

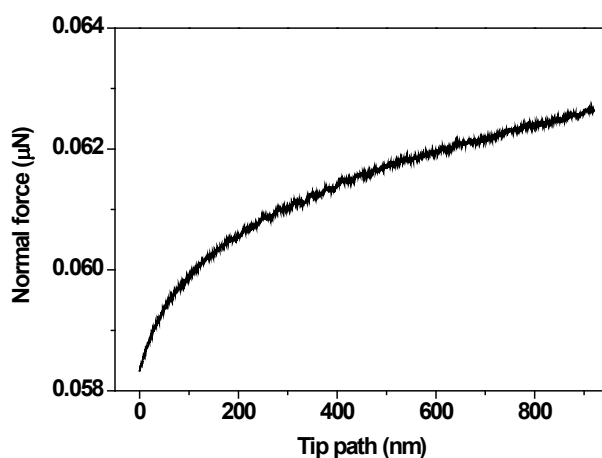


Figure S7. Normal force as a function of the AFM tip path corresponding to the fracture of the individual ox-MWCNTs@i-POP hybrid nanotube showed in **Figure 4**.

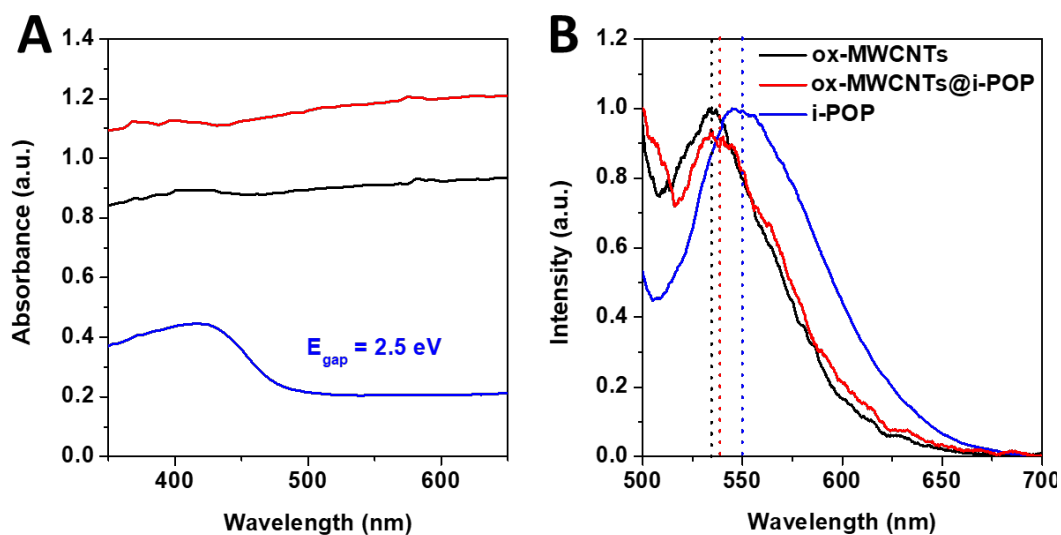


Figure S8. Optical properties of of ox-MWCNTs (black curve), ox-MWCNTs@i-POP (red curve) and i-POP (blue curve): a) absorption spectra and b) emission spectra.

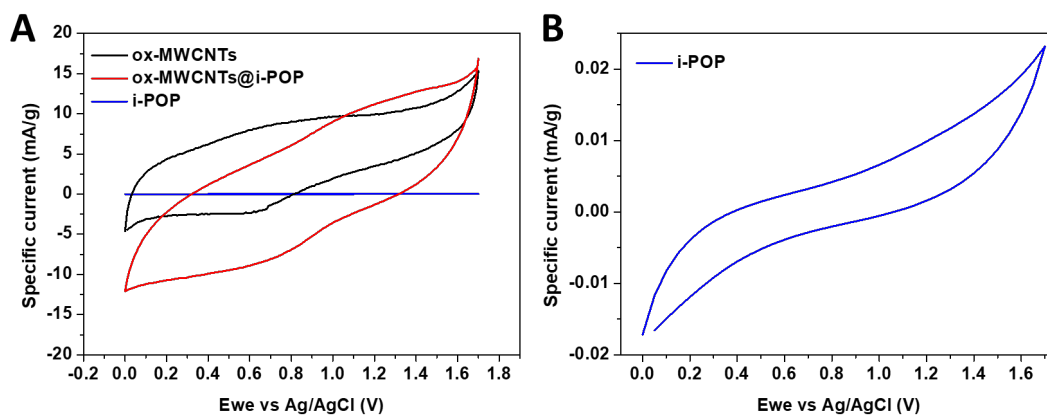


Figure S9. Electrochemical cyclic voltammeteries of the of ox-MWCNTs (black curve), ox-MWCNTs@i-POP (red curve) and i-POP (blue curve) materials tested at a scan rate of 50 mV/s.

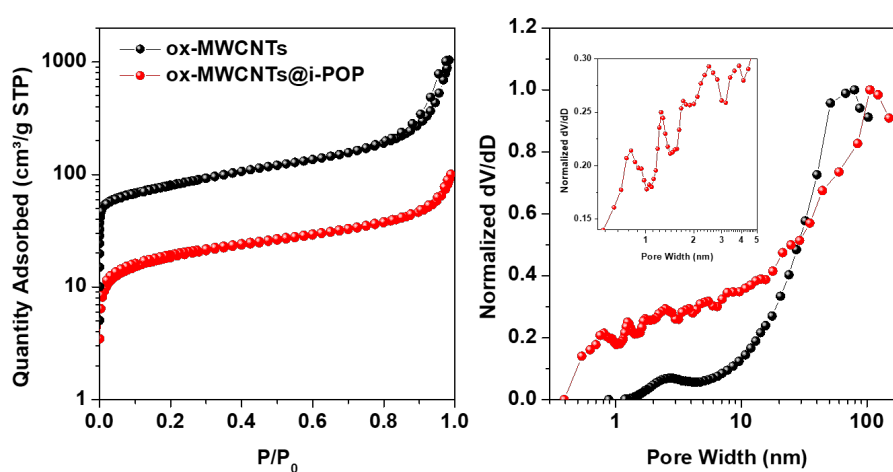


Figure S10. N₂ adsorption isotherms (left) and pore size distribution (right) of ox-MWCNTs and ox-MWCNTs@i-POP hybrid material.

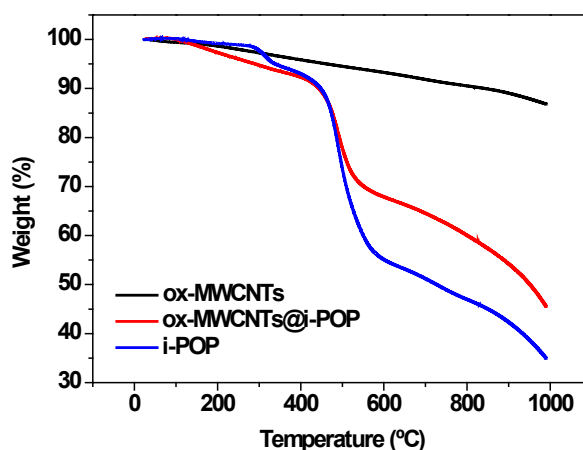


Figure S11. Thermogravimetric decomposition curves under Ar atmosphere.

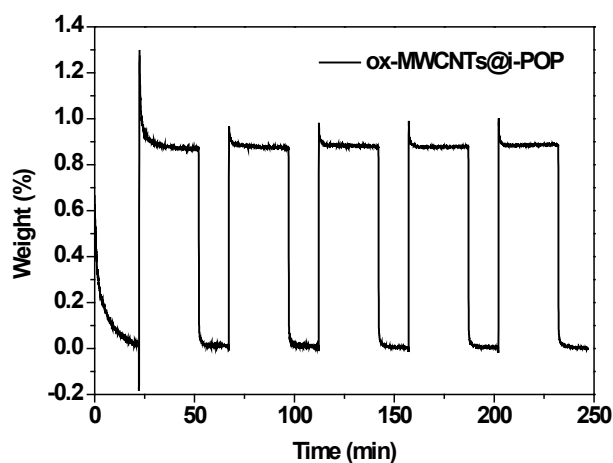


Figure S12. Cycling test of the CO₂ adsorption on the ox-MWCNT@i-POP hybrid material.

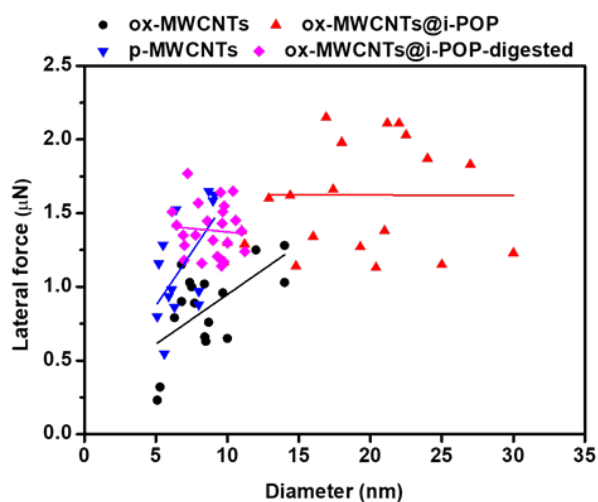


Figure S13. Effect of the diameter in the lateral force for cutting nanotubes of ox-MWCNTs, ox-MWCNTs@i-POP, p-MWCNTs and ox-MWCNTs@i-POP-digested.

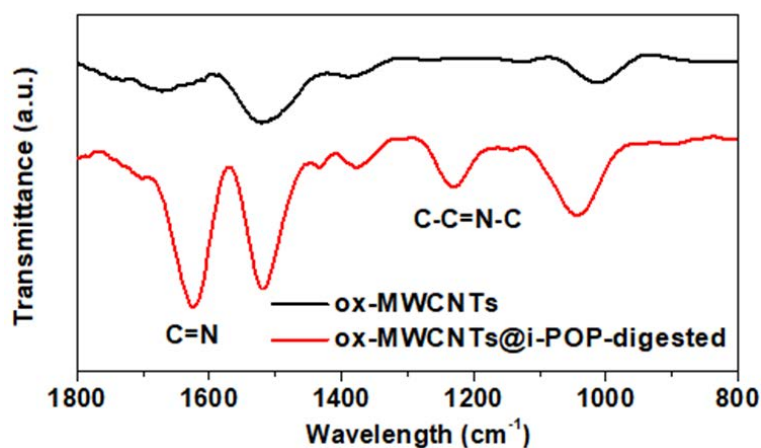


Figure S14. FT-IR spectra of ox-MWCNTs (black curve) and hybrid treated with aniline (red curve).

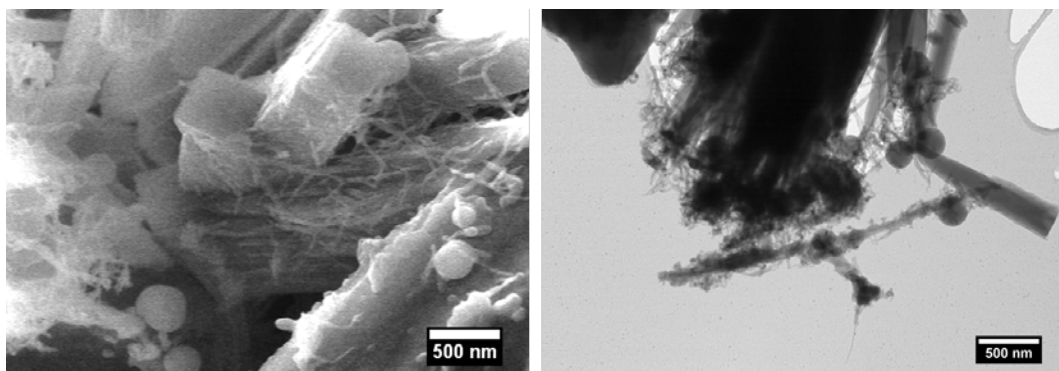


Figure S15. SEM and TEM image of the control sample referred as p-MWCNTs@i-POP.